Real-time spectroscopic ellipsometry of plasmonic nanoparticle growth in polyvinyl alcohol thin films

Patrick Kfoury, Yann Battie, Aotmane En Naciri, Laurent Broch, Michel Voue, Nouari Chaoui

▶ **To cite this version:**

Patrick Kfoury, Yann Battie, Aotmane En Naciri, Laurent Broch, Michel Voue, et al.. Real-time spectroscopic ellipsometry of plasmonic nanoparticle growth in polyvinyl alcohol thin films. Journal of Nanoparticle Research, 2024, 26 (2), pp.23. 10.1007/s11051-024-05937-0 . hal-04450913

HAL Id: hal-04450913
https://hal.science/hal-04450913v1

Submitted on 10 Feb 2024

HAL is a multi-disciplinary open access archive for the deposit and dissemination of scientific research documents, whether they are published or not. The documents may come from teaching and research institutions in France or abroad, or from public or private research centers.

L'archive ouverte pluridisciplinaire **HAL**, est destinée au dépôt et à la diffusion de documents scientifiques de niveau recherche, publiés ou non, émanant des établissements d'enseignement et de recherche français ou étrangers, des laboratoires publics ou privés.

Realtime spectroscopic ellipsometry of plasmonic Nanoparticles growth in PolyVinyl Alcohol thin films.

Patrick KFOURY[a], Yann BATTIE[a*], Aotmane EN NACIRI[a], Laurent BROCH[a], Michel VOUE[b], and Nouari CHAOUI[a]

a : LCP-A2MC, Université de Lorraine, ICPM, 1 Bd Arago 57070 Metz, France

b : LPMO, Université de Mons, Institut de Recherche en Science et Ingénierie des Matériaux, Place du Parc, 20, 7000 Mons, Belgium

* Yann.Battie@Univ-Lorraine.fr

Abstract

The thermal growth of silver nanoparticles (Ag NPs) embedded in Poly-vinyl alcohol thin films is studied as a function of annealing time by in-situ spectroscopic ellipsometry in the visible spectral range. Each recorded spectrum is analyzed by the Shape Distributed Effective Medium Theory model from which are determined the time evolutions of the film thickness, the shape distribution, the volume fraction of the nanoparticles and the effective dielectric function of the nanocomposite film. The estimated shape distribution shows that the nanoparticles remain almost spherical in the course of the annealing process in good agreement with the electronic microscopy examinations of the samples. As expected, the films exhibit a plasmon resonance band, the amplitude of which increases during the annealing while the film thickness decreases. The growth mechanism of the silver NPs was also investigated by analyzing the variation of their volume fraction in the films. The obtained results show that the NPs growth occurs via a mechanism involving Ag atoms (monomers) additions and/or reduction of Ag ions directly onto the AgNPs surface.

Keywords: Plasmonic Nanoparticles Growth, Nanoparticles Shape Distribution, In-situ Spectroscopic Ellipsometry, Growth Kinetics

Introduction

Silver nanoparticles (Ag NPs) exhibit plasmon resonances induced by the collective oscillations of their free electrons whose position depends on the size of the Ag NPs, their shape and their host medium[1]. Therefore, the growth of Ag NPs in dielectric thin films can give rise to nanocomposite materials with interesting optical properties and applications such as sensors[2], photovoltaic cells[3], non-linear optical activity-based devices[4], SERS[5], and optical filters[6]. Since the optical properties of the nanocomposites are particularly sensitive to the morphological properties of the embedded NPs, understanding their growth mechanism is crucial to generate nanocomposites with controlled properties.

Several synthesis routes have been proposed to elaborate Ag NPs embedded in dielectric thin films from the reduction of silver ions[7–19]. Porel *et al.*[10] were the first to introduce a simple experimental protocol to elaborate plasmonic NPs in polymer films, which consists in depositing a aqueous solution of polymer and metallic salts onto a solid substrates by casting or spin-coating and thermally reducing the metallic salts. In-situ monitoring of the NP growth would help to understand the growth kinetics and mechanism. As a non-invasive and in situ

optical diagnostic technique, spectroscopic ellipsometry has proven to be a very effective tool to monitor the growth NPs in polymer matrices. Oates *et al.*[20–22] succeeded in determining the time evolution of the mean radius of NPs growing in a polymer thin films by analyzing the ellipsometric spectra with the Maxwell Garnett theory. Voué *et al.*[23] conducted similar experiments in the UV-near IR spectral range but using a Lorentz oscillator. However, the theoretical approaches reported by these authors do not take into account the shape distribution of the NPs, which can have a significant impact on the optical response of this kind of systems[24]. Therefore, further investigation is required on the influence of the NPs shapes on the plasmonic properties of this kind of nanocomposite material. Recently, we have introduced a new effective medium theory called Shape Distributed Effective Medium Theory (SDEMT) to model the optical properties of a collection of ellipsoidal NPs which exhibits a shape distribution[25]. This model was successively used to extract the shape distribution of silver and gold NPs from their absorption or ellipsometric spectra[24–28]. In this paper, spectroscopic ellipsometry is used to monitor the growth of Ag NPs in PVA thin films. The SDEMT theory is applied to analyze the ellipsometric spectra recorded during the annealing of the films in order to determine the time evolution of the layer thickness, the volume fraction of Ag NPs and their shape distribution. The growth kinetics and possible mechanisms are discussed on the basis of the experimental results and their modelling by the SDEMT.

Materials and Methods

The silicon substrates were cleaned first in an ultrasonic bath of a mixture of soap and distilled water during 30 min, then in an ultrasonic bath of distilled water during 15 min. After that, the substrates are immersed 15 min in an ultrasonic bath of acetone, and finally 15 min in ethanol.

A 0.1g/ml PVA (MW: 13000 – 23000, Sigma Aldrich) aqueous solution (S0) was first prepared under vigorous stirring during 1h at 90°C and 23h at room temperature. A solution (S-PVA0) of 0.08g/ml of PVA was prepared by diluting (S0) with water with a 4 to 1 ratio. The resulting solution was then deposited on a cleaned silicon substrate by spin-coating at a rotation speed of 5000 rpm. The obtained film was then dried by spinning at 500 rpm for 2 min. The thickness of the PVA film as measured by spectroscopic ellipsometry was 196 ± 1 nm.

Solutions of PVA 0.08g/ml containing silver nitrate ($AgNO_3$, 99.995%, Alfa Aesar) were also prepared and deposed on a silicon substrate by spin coating at 5000 rpm. Three different samples named AG1, AG2, and AG3 with different Ag/PVA ratio were prepared. For the sample AG1, an aqueous solution (S1) of silver nitrate 0.158 ± 0.001g/ml was prepared. After stirring, the solutions (S0) and (S1) were mixed and stirred in a 4 to 1 ratio as way to obtain a new solution (S-AG1) with a PVA to water ratio of 0.08g/ml and a silver ions to PVA mass ratio of 25%. For the samples AG2, AG2-a, AG2-b, AG2-c and AG2-d, a solution (S2) of silver nitrate 0.400 ± 0.001g/ml was prepared. Then solutions (S0) and (S2) were mixed in a 4 to 1 ratio and stirred to obtain the solution (S-AG2) with a PVA to water ratio of 0.08 g/ml and a silver ions to PVA mass ratio of 63%. For the sample AG3, a solution (S3) of silver nitrate 0.600 ± 0.001g/ml was prepared. After stirring, the solutions (S0) and (S3) were mixed

and stirred in a 4 to 1 ratio as way to obtain a new solution (S-AG1) with a PVA to water ratio of 0.08g/ml and a silver ions to PVA mass ratio of 95%.

Table 1 shows a comparison between samples AG1, AG2, and AG3 in terms of nominal mass ratios (r), volume fractions (f) of silver ions with respect to PVA, and their initial thicknesses estimated by spectroscopic ellipsometry.

Table 1: Nominal value of the mass ratio (r) and volume fraction between Ag+ and PVA of AG1, AG2, and AG3. The film thickness h is determined from ellipsometric measurements recorded before the annealing

Sample	r (%)	f (%)	h (nm)
AG1	25.0 ± 0.2	3.0 ± 0.1	156 ± 1
AG2	63.0 ± 0.4	7.0 ± 0.1	195 ± 1
AG3	95.0 ± 0.3	10.2 ± 0.1	225 ± 2

The PVA0 sample was annealed at 110°C for 2h, and the samples AG1, AG2, and AG3 were annealed at 110°C for 8h on the substrate holder of the ellipsometer equipped with a Linkam (THM-ELLIPS Low stage) heating stage. The heating rate was 5°C/min starting from 25°C to 110°C. During the thermal annealing, real-time ellipsometric spectra were recorded at an angle of incidence of $65.5° \pm 0.5°$ for all samples by using a homemade Real-Time Spectroscopic Rotating Compensator Ellipsometer[29, 30] (RTSRCE). The angle of incidence was precisely determined by fitting the first spectra recorded at room temperature. The ellipsometer (Fig.1) is composed of a supercontinuum white light laser source (Leukos SM-30-UV), a Rochon polarizer, and an achromatic rotating quaterwave plate. The reflected light is split into two perpendicularly polarized beams by a second Rochon polarizer. These two separate beams are simultaneously analyzed by two synchronized CCD detectors, providing final spectrum of averaged ellipsometric spectra free of systematic errors [30].

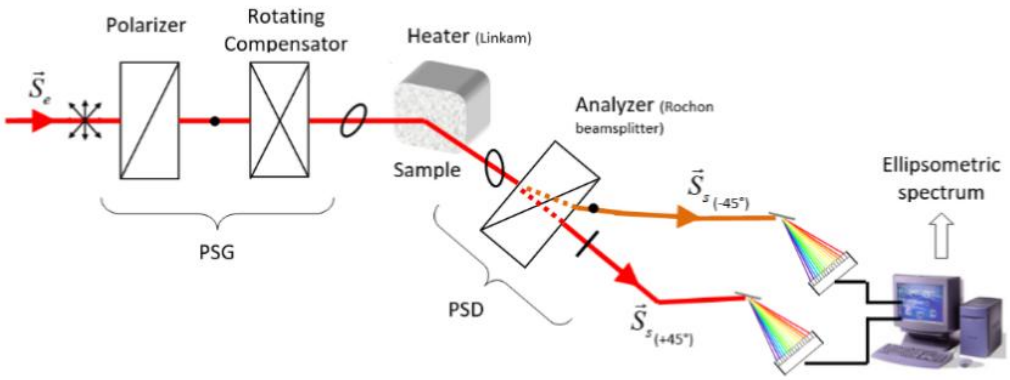

Figure 1: Scheme of the Realtime Spectroscopic Rotating Compensator Ellipsometer coupled with the Linkam heater.

Ellipsometric angles Ψ and Δ , as defined in equation 1, were collected in the 450 - 800 nm range and averaged over 10 scans resulting in a sampling rate of 1 spectrum every 390 ms.

$$\rho = \frac{r_p}{r_s} = tan\Psi e^{i\Delta}, \quad (1)$$

r_p and r_s are the Fresnel reflection coefficients for p-polarized and s-polarized light respectively, and ρ is the complex reflectance ratio of the system. Then, one spectrum over 15 was modeled which results in a calculated data point every 5.85s. The other spectra are discarded to reduce the modeling time. The ellipsometric spectra analysis is performed on Is and Ic parameters which are functions of Ψ and Δ according to the following equations:

$$Is = \sin 2\Psi \sin \Delta \quad (2)$$

$$Ic = \sin 2\Psi \cos \Delta \quad (3)$$

Samples AG2-a, AG2-b, AG2-c, and AG2-d were annealed on the same heating stage at 110°C for 30, 60, 120, and 180 min respectively without optical characterization. The heating rate was also 5°C/min starting from 25°C to 110°C.

After cooling to room temperature, the films were scrapped with a razor blade and the fragments are then plunged in water and recovered on a copper grid coated with holey carbon film. Finally, Scanning Transmission Electron Microscopy (STEM) images of the NPs inside the PVA matrix were recorded using a Zeiss Supra 40 Scanning Electron Microscope (SEM) operating in transmission mode at 30 kV.

Ellipsometric modeling

Figure 2 shows the model used to analyze the ellipsometric spectra of samples PVA0, AG1, AG2 and AG3. The samples were modeled as a silicon substrate covered by a PVA layer (for sample PVA0) or an Ag-PVA nanocomposite layer (for samples AG1, AG2, and AG3) with air taken as the ambient medium and neglecting the contribution of the native oxide layer. The ellipsometric spectra were calculated according to the Abeles formalism[31]. The dielectric function of silicon was extracted from the literature[32] and the dielectric function of PVA was modeled by a non-absorbent Lorentz oscillator dispersion law :

$$\varepsilon = \varepsilon_\infty + \frac{(\varepsilon_s - \varepsilon_\infty)\omega_0^2}{\omega_0^2 - \omega^2}, \quad (4)$$

where ε_∞=1.844, ε_s=2.277 and ω_0=7.78 eV are the dielectric constant at infinite frequency and the static dielectric constant and the resonance energy of the Lorentz oscillator, respectively. These parameters were determined by fitting simultaneously the ellipsometric spectra of

almost 10 PVA layers of different thicknesses ranging from 50 to 300 nm deposited on silicon substrates.

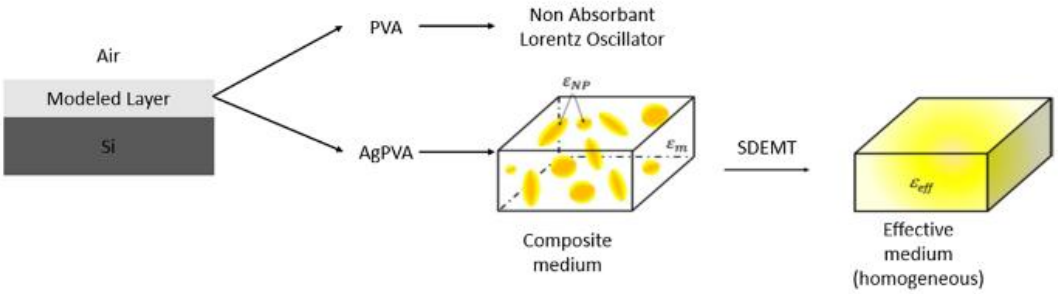

Figure 2: Model used to analyze ellipsometric spectra

Fig. 3 shows a comparison between the obtained PVA dispersion law and those given in the literature by Schnepf *et al.*[33] and Guyot *et al.*[34]. The dispersion law obtained in this work is similar to that proposed by Guyot *et al.*[34]. The slight discrepancy with the dispersion reported by Schnepf *et al*. might be due to the different molecular weights and hydrolysis degree of the PVA used by these authors.

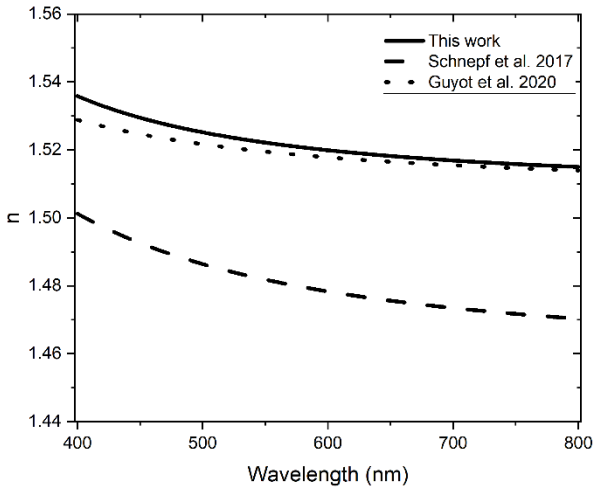

Figure 3: Comparison between the refractive index of PVA used in this paper (solid line) and those reported by Schnepf et al.[26] (dashed line), and by Guyot et al.[27] (dotted line).

The description of the optical properties of the Ag-PVA layer requires to take into account the shape distribution of the NPs. Indeed, as shown by several authors[1, 35–37], the plasmonic resonances of Ag NPs are strongly related to their morphology. Thus, in our modeling approach, we considered the Ag-PVA layer as a homogeneous medium composed of ellipsoidal NPs distributed in shape. This nanocomposite is described by an effective

dielectric function (ε_{eff}) according to the Shape Distributed Effective Medium theory (SDEMT)[24]

$$\varepsilon_{eff} = \frac{(1-f)\varepsilon_m + f\varepsilon_{np}<\beta>}{(1-f)+f<\beta>}, \quad (5)$$

with $\beta(L_1, L_2) = \frac{1}{3}\sum_{i=1}^{3} \frac{\varepsilon_m}{\varepsilon_m + L_i(\varepsilon_{np} - \varepsilon_m)}$. (6)

f, ε_m and ε_{np} are the volume fraction of Ag NPs, the dielectric function of the PVA matrix and the dielectric function of the silver NPs[32], respectively. In the following, we neglect the confinement effect which occurs for NP size smaller than 2 nm[38]. $L_1 \leq L_2 \leq L_3$ are the depolarization parameters which respect the following sum rule:

$$\sum_{i=1}^{3} L_i = 1. \quad (7)$$

These parameters, which vary in the 0-1 range, only depend on the ellipsoidal shape of each NP. Each of them is equal to 1/3 for a spherical particle. In the following, we assume that the distribution of depolarization parameters is described by a gaussian distribution:

$$P(L_1, L_2) = Ce^{-0.5\sum_{i=1}^{3} \frac{(L_i - \bar{L}_i)^2}{\sigma_i^2}}. \quad (8)$$

C is a normalization constant. $\bar{L}_i$ and σ_i are the mean value and the standard deviation of the depolarization parameter L_i, respectively. This distribution of depolarization factor $P(L_1, L_2)$ can be converted into a distribution of aspect ratios of ellipsoidal NPs by applying the following coordinate transformation:

$$L_i = \frac{r_2 r_3}{2} \int_0^{+\infty} \frac{dq}{(q + r_i^2)\sqrt{\prod_{i=1}^{3}(q + r_i^2)}}, \quad (9)$$

where $r_i = \frac{a_i}{a_1}$ the 3 aspect ratios and $a_3 \leq a_2 \leq a_1$ the length of the principal axes of each ellipsoidal NP.

As a result, the mean value of β is given by:

$$< \beta > = \iint P(L_1, L_2)\beta(L_1, L_2)\, dL_1 dL_2. \quad (10)$$

Results and discussion

PVA0 Sample

Figure 4 a,b,c shows the Is and Ic ellipsometric spectra of PVA0 measured for three annealing times. The slight variations in the Is and Ic spectra as a function of annealing time indicate a change in the dielectric function and/or thickness of the PVA layer. To discriminate both effects, the evolutions of the measured ellipsometric angles at a wavelength of 500 nm are presented together in a Ψ-Δ chart (Figure 5) with three simulated iso-refractive[39] index curves. The film thickness varies along an iso-refractive index curve. A similar approach has been proposed by Guyot *et al*. to investigate the growth of gold nanoparticles in the same polymer matrix[40]. As illustrated in Figure 5, the measured ellipsometric data are located along the iso-refractive index curve of 1.5 suggesting that the refractive index of the PVA layer remains almost constant during the annealing. Therefore, it can be concluded that the variations of the ellipsometric spectra are related to a decrease of the thickness of the PVA film.

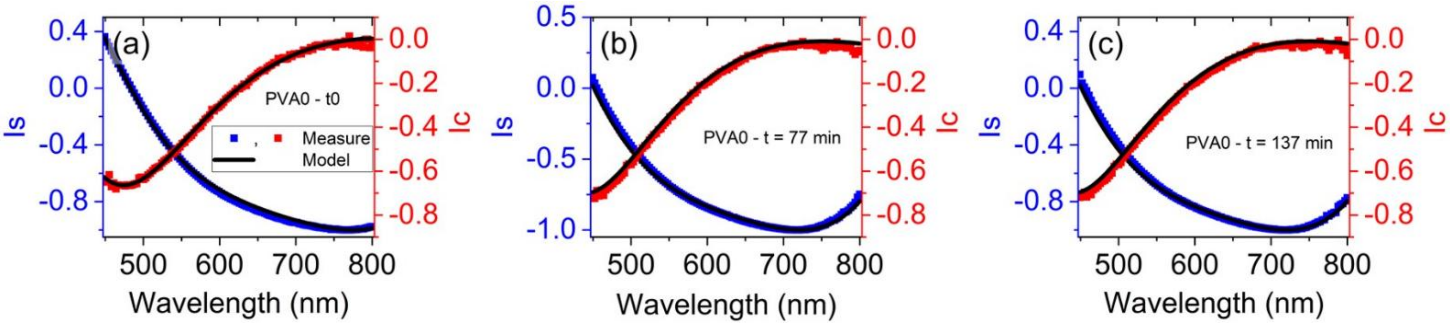

Figure 4: Comparison between the measured and fitted Is and Ic spectra of PVA0 for annealing time of (a) 0 min, (b) 77 min, and (c) 137 min.

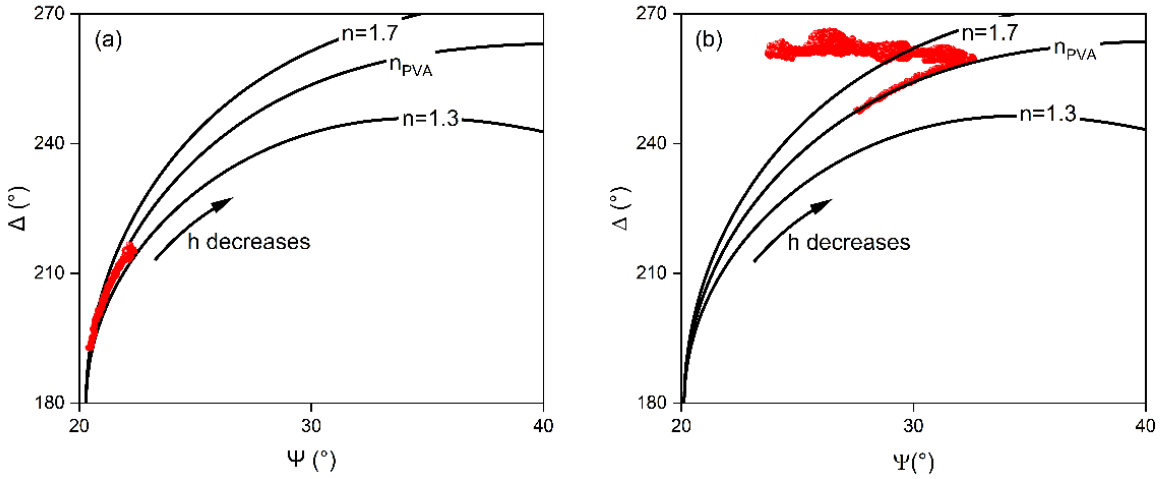

Figure 5: Representation in a Ψ–Δ chart of the evolution of the ellipsometric angles of (a) PVA0, and (b) AG2 measured at a wavelength of 500 nm (red dots). Three iso-refractive index curves (n=1.3, n=n_{PVA} and 1.7) are represented as black solid lines. Time increases as h decreases.

The film thickness of the PVA film was then fitted by using the Levenberg-Marquart algorithm (Fig.4, solid lines). The model reproduces satisfactorily the experimental data with a root mean square error smaller than 0.067. Considering the variation range of Is and Ic, this result suggests that the relative error is smaller than 3.5%. The film thickness of the PVA was plotted as a function of annealing time in Figure 6. It is observed that the thickness decreases with annealing time by about 7 % after two hours. This thickness decrease can be explained by the evaporation of residual water inside the polymer layer [41]and/or by the relaxation of the mechanical stresses induced by the spin coating process in the film.

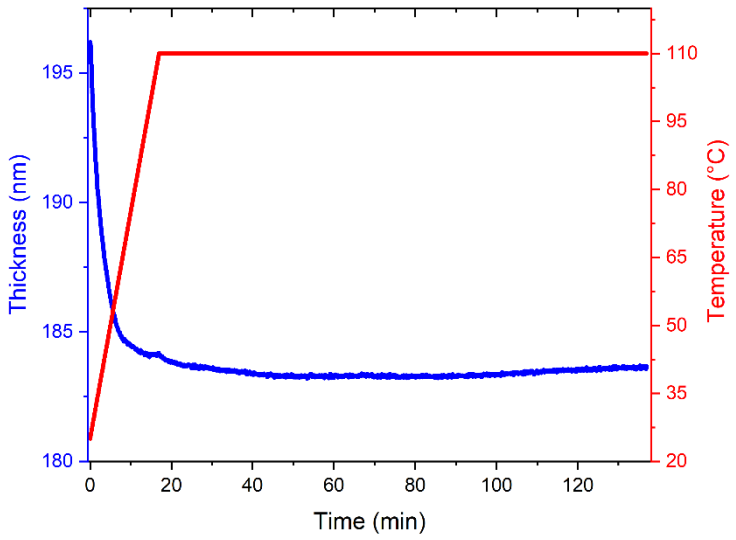

Figure 6: Evolution of the PVA0 film thickness during the annealing

The impact of the annealing on the ellipsometric spectra of PVA film was further studied for the films containing silver ions (samples AG1, AG2, and AG3). As shown in figure 5 (b), the variations of Ψ and Δ (red points) measured on sample AG2 are more complex than those observed for sample PVA0 (Fig. 5(a)). Similar results are obtained for AG1 and AG3 (not shown). First, the evolutions of these two parameters do not follow the iso-refractive index curves suggesting that the annealing process induces change in both film thickness and complex refractive index. This behavior can be related to the thermal growth of silver NPs in the PVA matrix[21]. To corroborate this result, STEM images of Ag NPs in samples AG1, AG2, and AG3 (Fig. 7), were recorded after eight hours annealing at 110°C. The number-weighted distribution of the mean Feret diameter of the AgNPs was determined from these images. The obtained NPs size distributions can be described by a lognormal law. The three samples present similar NPs size distribution with modes of 7 nm for AG1 and 9 nm for both AG2 and AG3. The aspect ratio distributions of the AgNPs in samples AG1, AG2 and AG3, defined as the ratio between the minimal and the maximal Feret diameter were determined and presented in Figure 7(g)(h)(i). For the three samples, the aspect ratio distributions exhibit a single mode located at 0.75 showing that the NPs are almost of spherical shape. These

results reveal the weak influence of the initial Ag ions concentration on both size and shape of AgNPs in the PVA matrix.

In order to gain insight into the growth mechanism of the AgNPs into the PVA matrix, the influence of the annealing duration on the NPs growth at 110°C is examined. STEM observations of samples, similarly prepared as sample AG2, were carried out after 30 (AG2-a), 60 (AG2-b), 120 (AG2-c), and 180 min (AG2-d) annealing durations at 110°C (Fig. 8). Whatever the annealing duration (Fig.8(i)-(l)) the aspect ratio presents a mode at 0.85, suggesting that the NPs remain of spherical shape throughout the whole growth process. In addition, as shown in the inset of Fig. 8(d), few large faceted NPs are observed. The distribution of the mean Feret diameter follows, in the case of AG2-a a normal distribution with a mode of 25 nm and a standard deviation of 10 nm. At longer annealing duration, the mean Feret diameter distribution follows a lognormal distribution. The STEM images and the parameters of the lognormal distributions reveal an increase of the fraction of AgNPs with diameter less than 20 nm with increasing annealing duration. The distribution histograms are based on a total count between 7000 and 13000 NPs for samples AG1, AG2, and AG3, and between 400 and 3000 NPs for samples AG2-a through AG2-d.

The observed large NPs with size above 20 nm at the early stage of the annealing treatment (Fig. 8(a)) are likely generated during the sample preparation. Indeed, a non-zero volume fraction is calculated at $t = 0$ min for AG1. These NPs may constitute the fraction of previously described large facetted NPs (Fig. 8 (d)) after further growth. Another scenario can be invoked for the formation of this large NPs population. These NPs could also be formed in the PVA film porosities which contain rests of the non-evaporated silver ions solution. This could explain the large particles population observed at the early stage of the annealing process (Fig. 8(a)) as well as the large faceted particles observed at the end of the process. These large NPs may grow via a supersaturation of Ag ion solution due to solvent evaporation, i.e. growth in liquid medium [42]. This scenario is consistent with the high growing rate of these particles compared to those supposed to grow in the PVA matrix. Note also that these AgNPs are already observed after 30 min. annealing (Fig. 8(a)) which is also the time required to reach the minimum thickness of the film according to Fig. 6. This supports the hypothesis that these large AgNPs grow in the liquid trapped in the PVA film pores.

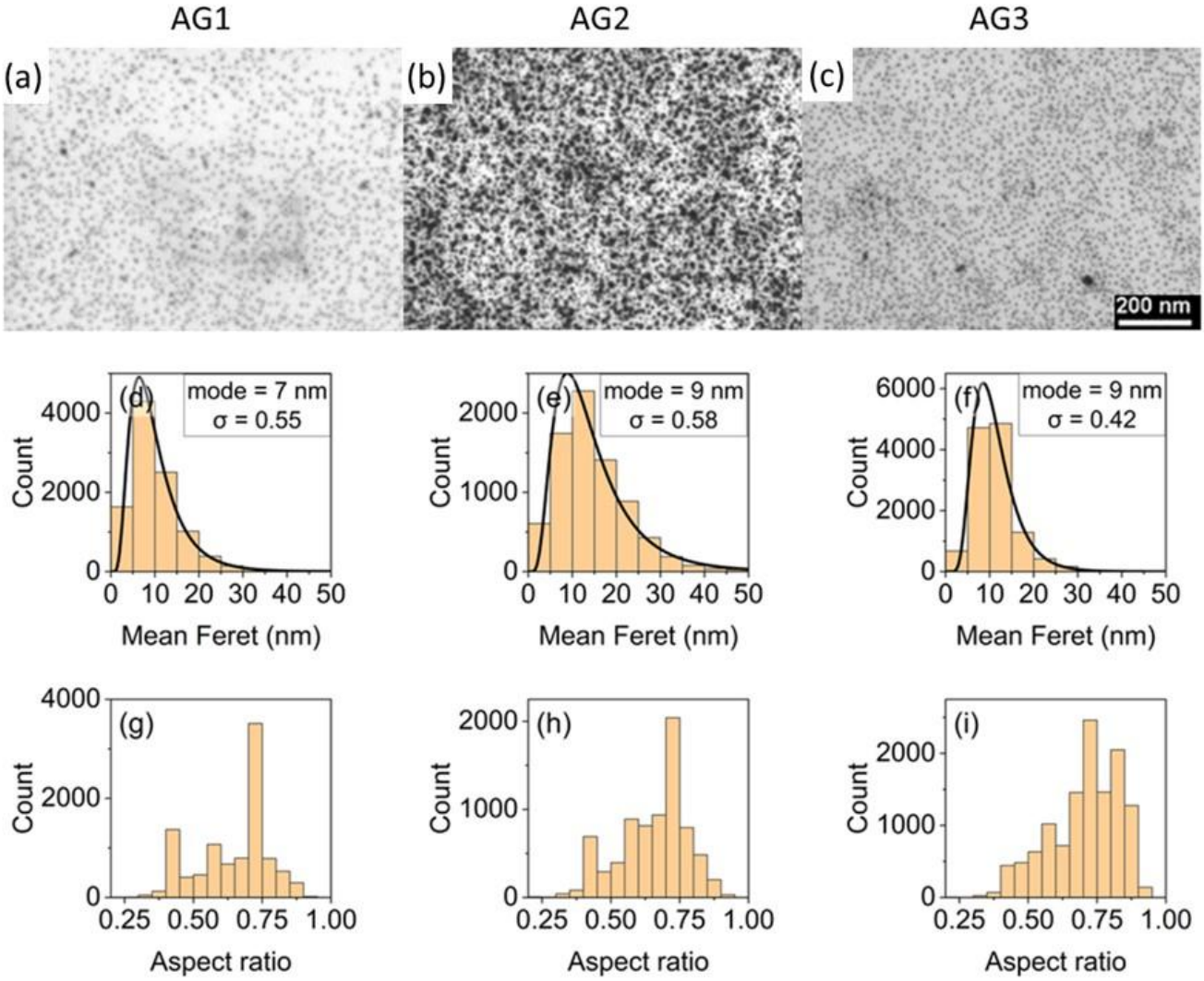

Figure 7: (a)(b)(c) STEM images, (d)(e)(f) distributions of mean Feret diameter and (g)(h)(i) distributions of aspect ratio of (a)(d)(g) AG1, (b)(e)(h) AG2, and (c)(f)(i) AG3 silver NPs.

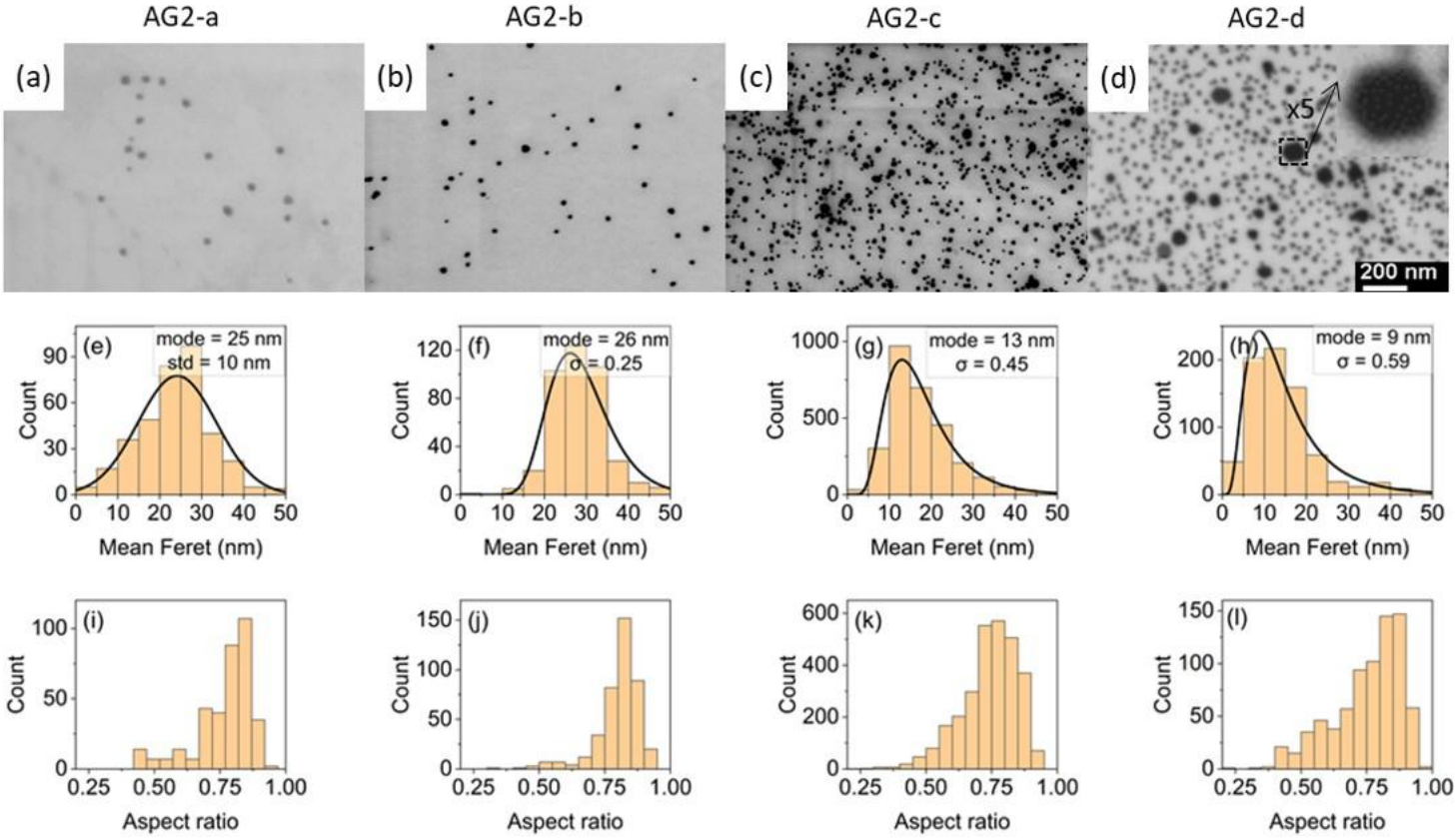

Figure 8: (a)(b)(c)(d) STEM images, (e)(f)(g)(h) mean Feret diameter distributions and (i)(j)(k)(l) aspect ratio distributions of (a)(e)(i) AG2-a, (b)(f)(j) AG2-b, (c)(g)(k) AG2-c, and (d)(h)(l) AG3-d silver NPs. In inset of (d) a X5 magnified image of a AG2-d faceted NP.

Since STEM is poorly adapted for *in situ* monitoring the evolution of NPs shape distribution during their growth, the use of spectroscopic ellipsometry as a non-invasive *in situ* characterization tool is proposed to further investigate the thermal growth of the AgNPs in the PVA films. The recorded spectra of samples AG1, AG2 and AG3 at the end of the annealing process were first analyzed by fitting the film thickness h and all the parameters of the SDEMT model ($\sigma_1, \sigma_2, \sigma_3, \overline{L_1}, \overline{L_2}$ and f). In good agreement with the STEM observations, and whatever the starting parameters (see Table S1, Fig. S1, and Fig. S2 in Supporting Information), the shape distribution converged towards a spherically centered distribution given by:

$$P(L_1, L_2) = Ce^{-0.5\left(\frac{\left(L_1-\frac{1}{3}\right)^2+\left(L_2-\frac{1}{3}\right)^2}{\sigma_1^2}\right)}. \quad (12)$$

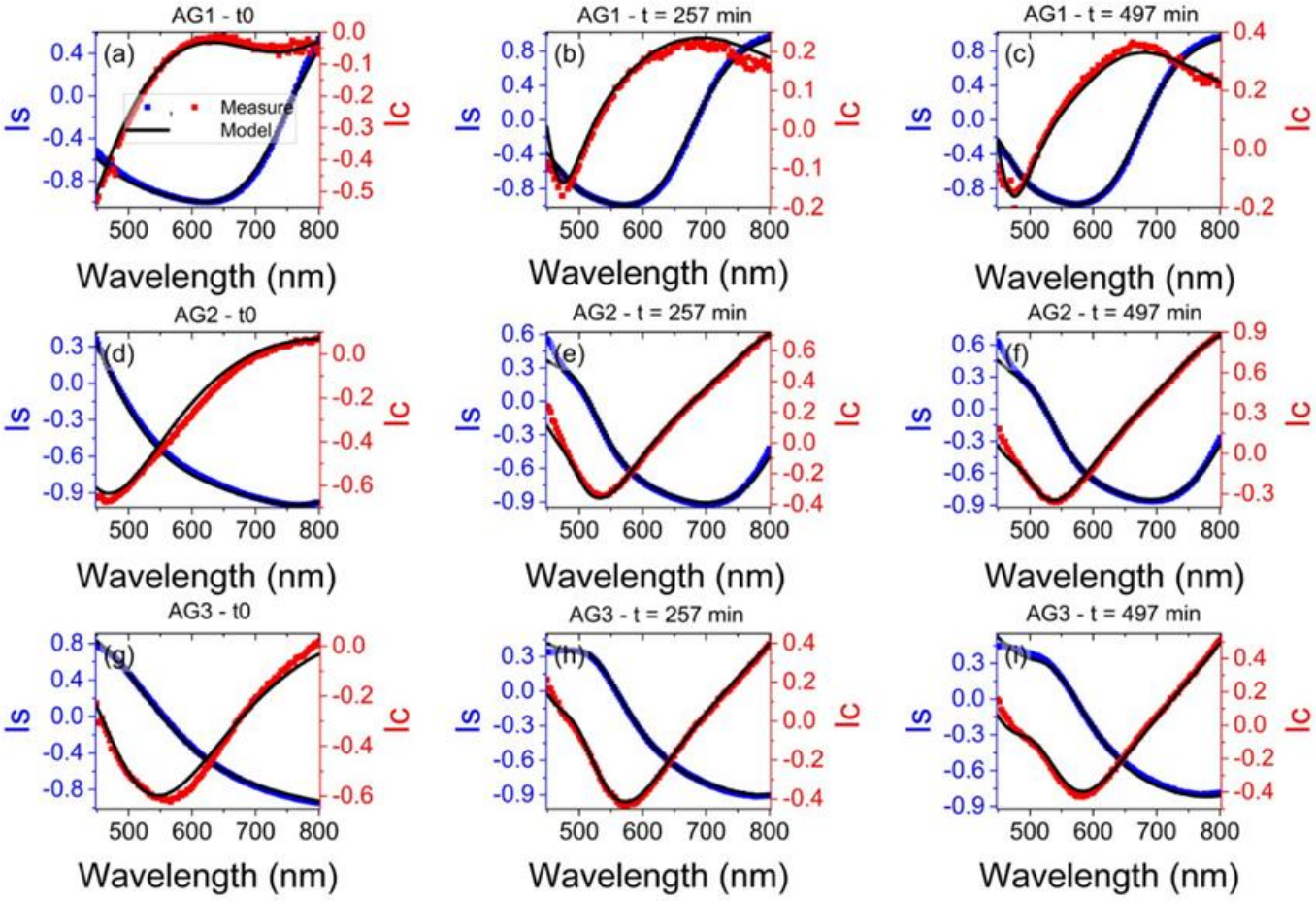

Figure 9: Comparison between the measured and modeled Is (blue) and Ic (red) spectra. (a)(b)(c), (d)(e)(f), and (g)(h)(i) represent samples AG1, AG2, and AG3 respectively. (a)(d)(g), (b)(e)(h), and (c)(f)(i) correspond to the annealing time of 0, 257 min, and 497 min respectively.

Therefore, by assuming this distribution applies during the whole annealing treatment, the number of free parameters can be reduced to 3 parameters: h, f, and σ_1. As illustrated in Fig. 9, the model reproduces all measured ellipsometric spectra with a root mean square error smaller than 0.034 for AG1, 0.055 for AG2 and 0.077 for AG3. In accordance with the

conclusion drawn from PVA0, here again, these results reveal a decrease of the film thickness during the annealing. The aspect ratio distributions of the NPs in samples AG1, AG2, and AG3 estimated from ellipsometric measurements recorded 497 min annealing duration at 110°C are reported in Fig. 10.

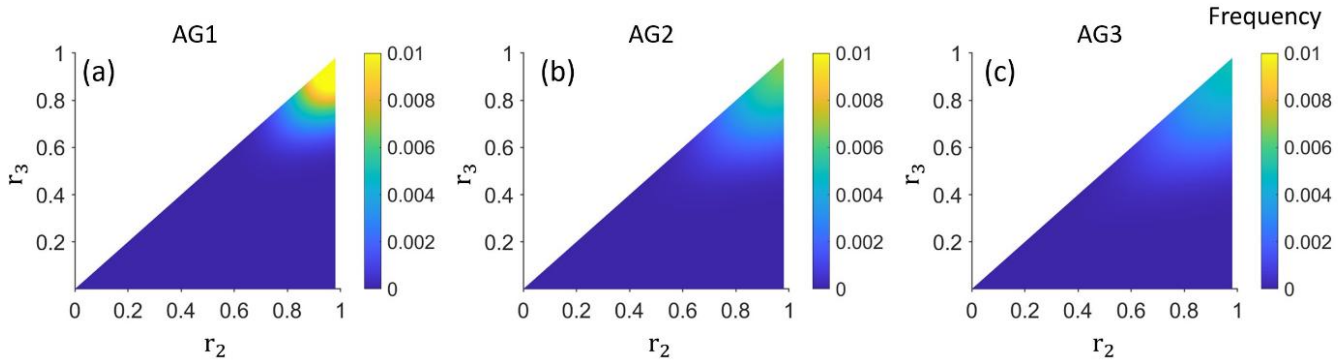

Figure 10: Distributions of aspect ratio of (a) AG1, (b) AG2, and (c) AG3 NPs estimated by spectroscopic ellipsometry for a 497 min annealing time.

Fig.11 shows the aspect ratio distributions of NPs as calculated by the SDEMT in sample AG2 for 30, 60 120, 180, and 480 min annealing durations at 110°C. In good agreement with STEM observations, these results reveal the independence of the NPs aspect ratio distribution on both silver ion concentration and annealing duration. However, in contrast with STEM observations, ellipsometry is a nonlocal characterization tool, and the total count from which these distributions are obtained is much larger (10^{10}-10^{11} particles at the end of the annealing).

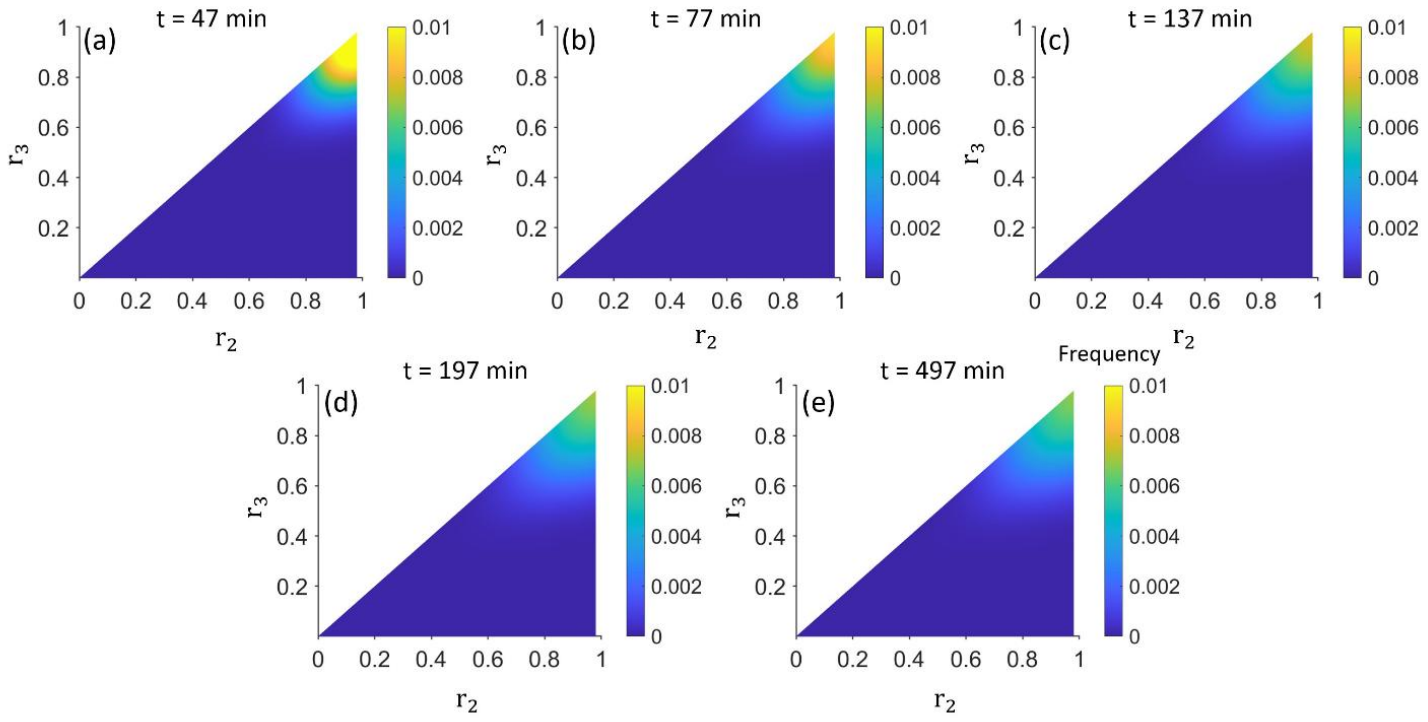

Figure 11: Distributions of aspect ratio of AG2 NPs estimated by spectroscopic ellipsometry for annealing time of (a) 30, (b) 60, (c) 120, (d) 180 and (e) 480 min at 110°C.

Fig. 12 shows the time evolution of the volume fraction of AgNPs estimated from the ellipsometric measurements. It is observed that the AgNPs detection threshold occurs at 110°C. In other words, their number and size are large enough to exceed the detection threshold of the ellipsometer. Indeed, according to simulations shown in Figure S3, the detection threshold, in terms of Ag volume fraction, is estimated to be about 0.075 %. In the early stage of the process the AgNPs volume fraction increases with a constant rate before reaching a plateau after, i.e. a growth rate decrease, about 5h-6h annealing duration. Note also that the final AgNPs volume fraction is consistent with the initial silver ions concentration (reported in Table 1) which means that almost all the silver ions are reduced to form AgNPs.

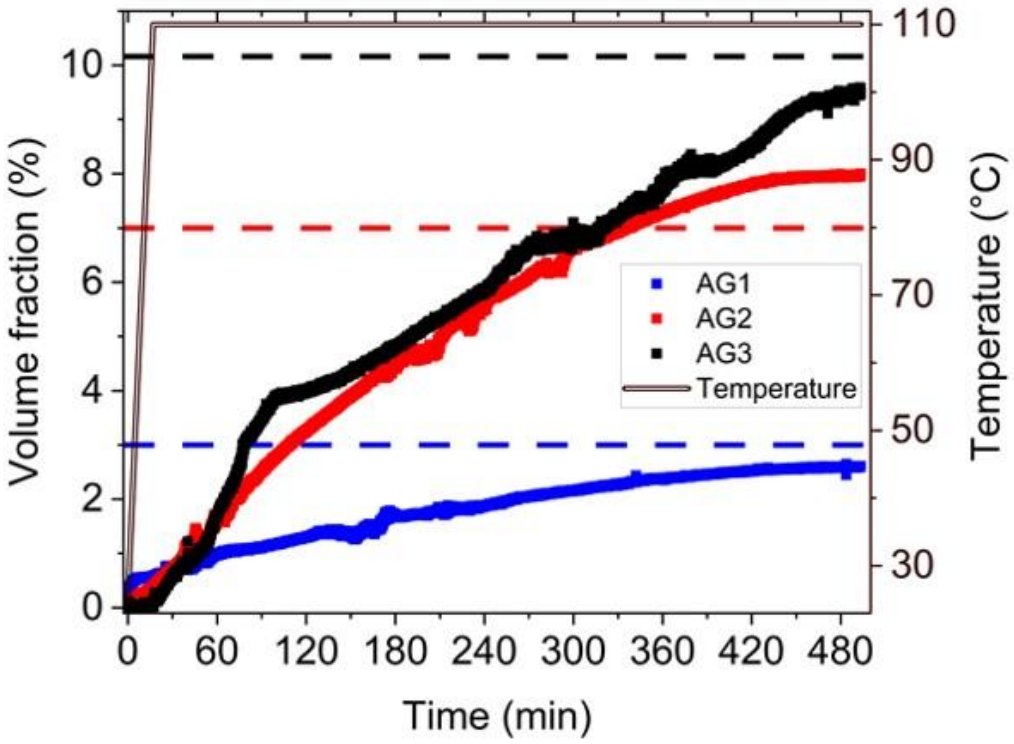

Figure 12: Evolution of the volume fraction of AG1, AG2, and AG3 NPs estimated by spectroscopic ellipsometry. Dashed lines represent the nominal volume fractions for each sample.

In the following, the effective dielectric function of the AG-PVA films obtained from spectroscopic ellipsometry was determined as a function of annealing duration at 110°C. For sake of clarity, only selected spectra are presented in Figure 13. The effective dielectric functions of AG1, AG2 and AG3 exhibit similar trends. At 110°C, a plasmon band appears in the imaginary part of the effective dielectric function. According to the Kramers-Kronig[43–45] relations, a large variation of the real part of the effective dielectric function is observed around the plasmon wavelength. According to the Fröhlich condition[46], this band, centered in the 430-460 nm range, can be assigned to spherical silver NPs. The amplitude of the plasmon band continuously increases during the annealing, revealing the growth of AgNPs. These results confirm the increase of the AgNPs volume fraction. Note that at the end of the annealing, the amplitude of AG3 plasmon band is 3 times higher than that of AG1 in good agreement with to the expected AgNPs volume fraction of these two samples[47]. Another noteworthy feature on Fig. 13 is the red shift of the plasmon resonance of about 30 nm with annealing duration and initial Ag ions concentration. Since, the AgNPs shape and size distribution remain almost the same, this redshift can be assigned to plasmonic interactions between the AgNPs[48].

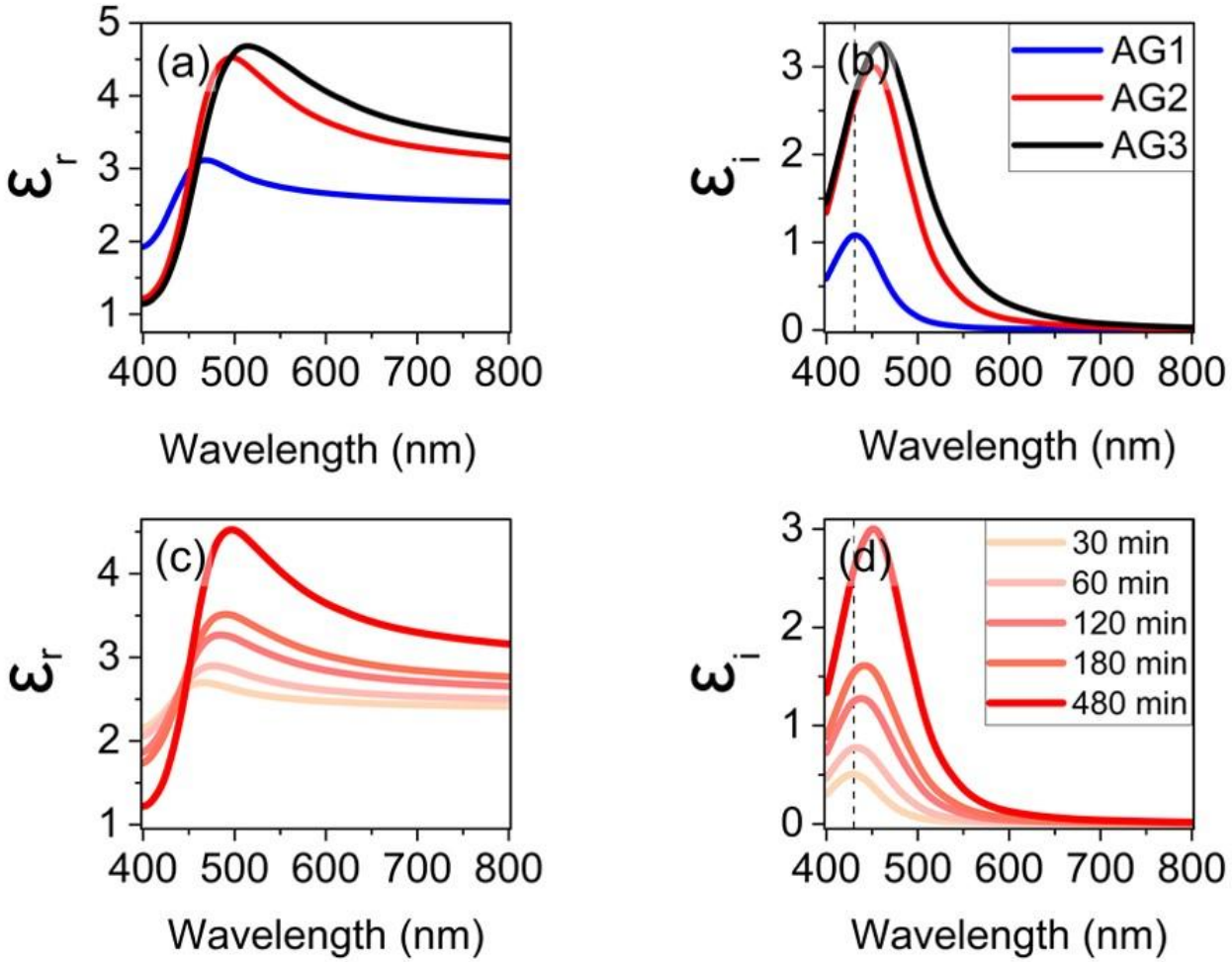

Figure 13: Blue, red and black lines represent samples AG1, AG2, and AG3 respectively. Degraded red lines represent sample AG2 at different annealing times. (a)(c) represent the real part of the effective dielectric function spectra. (b)(d) represent the imaginary part of the effective dielectric function spectra. Black dashed line corresponds to 430 nm, the resonance wavelength of AG1 (b) and AG2 after 30 min annealing at 110°C (d).

According to several authors [10, 40, 49], the formation of AgNPs in PVA film via a thermal process occurs in several steps.

The thermal annealing provides sufficient energy to promote the reduction of the silver ions by the -OH groups of the PVA[50]. As the annealing temperature exceeds the glass transition temperature of PVA (T_g=85°C)[51], the formation and growth of AgNPs is observed. As stated before, the observation of AgNPs occurs as soon as their volume fraction exceeds a threshold value that depends on the detection limit of the ellipsometer (see Fig. S3). Therefore, the initial steps of the AgNPs formation mechanism including silver reduction, molecular clusters and nuclei formations are out of scope of this experiment.

The findings of this work show that (i) whatever the initial silver ions concentration, the final AgNPs size distribution is lognormal and present a mode centered at about 10 nm (Fig. 7) (ii) the final AgNPs are spherical and remain spherical throughout the annealing duration (Fig. 7,8,10 and 11), (iii) the time evolution of the AgNPs volume fraction increases monotonously in a first stage and reaches a plateau at a volume fraction value close to the initial silver ion concentration (Fig.12), and (iv) plasmon band red shift is observed as the initial silver ions concentration (Fig. 13(b)) and/or the annealing duration increase (Fig. 13(d)).

The fact that the NPs remain spherical throughout the annealing process strongly suggests that the AgNPs growth occurs via a mechanism involving Ag atoms (monomers) additions and/or reduction of Ag ions directly onto the AgNPs surface. Growth via coalescence of AgNPs is thus highly improbable.

Furthermore, the observed plateau, i.e. decrease of the growth rate, at the end of the annealing process is consistent with a growth mechanism by diffusion of Ag atoms (and/or Ag ions) issued from the polymer matrix. The growth rate may decrease as a consequence of the depletion of Ag atoms/ions in the vicinity of the AgNPs. In this way, a simple calculation shows that the growth of a 10 nm diameter AgNPs would require about 3×10^4 Ag atoms and/or ions. Furthermore, in a Ag/PVA film prepared in a similar way to samples AG1 (3%) and AG3 (10%), assuming the ions are homogeneously distributed in the PVA matrix, the number of silver ions per cubic nanometer are 2 and 7 ions/nm^3, respectively. Therefore, an Ag "depleted volume" of 10^5 nm^3 for AG1 and 3×10^4 nm^3 for AG3 would be created around a 10 nm diameter AgNPs. This Ag "depleted volume" would correspond to a 29 and 19 nm diameter sphere around the AgNPs for AG1 and AG3, respectively. The edge to edge gap between the surface of two AgNPs would be 19 and 9 nm, respectively giving a ratio between g and the AgNPs radii of almost 3.8 and 1.8, for AG1 and AG3 respectively. This estimation may explain the red shift of the plasmon bands observed between AG1 and AG3 (Fig. 13(b)). Indeed, the AgNPs in AG1 are supposed to be sufficiently remote from each other to not interact whereas those in AG3 are supposed to be sufficiently closed to each other so that they are weakly coupled[52–54]. This assumption constitutes a reasonable explanation for the independence of the AgNPs size distribution on initial silver ions concentration and is also in good agreement with the increase of the AgNPs numbers with initial silver ions concentration.

Conclusion

In summary, real-time spectroscopic ellipsometry is used to investigate the thermal growth of silver NPs in PVA film. We show that the film thickness decreases during the annealing due to the evaporation of residual solvent and/or the relaxation of the mechanical stresses induced by the spin coating process in the film. By coupling the ellipsometric measurements with the SDEMT theory, we found that NPs are detected at 110°C. The growth rate is almost constant at the beginning of the NPs growth while it tends to decrease at the end of the annealing. In addition, the NPs shape distribution remains centered on the locus of spherical NPs during the annealing. It does not depend on the silver precursor concentration. This result which is confirmed from STEM measurement, suggests that the NPs growth is isotropic and does not involved any coalescence process. The redshift of the plasmon band observed during the annealing is related to the coupling between NPs. Larger NPs formed at the beginning of the annealing are faceted, confirming that these NPs are crystallized. We found that AgNPs growth occurs via a mechanism involving Ag atoms (monomers) additions and/or reduction of Ag ions directly onto the AgNPs surface.

Funding This work was supported by the PHC Tournesol Program (46237UL).

Conflict of Interest Authors declare no conflict of interest.

Authors' contributions These authors contributed equally to the work

Availability of data and material The datasets generated during and/or analysed during the current study are available from the corresponding author on reasonable request.

References

1. Yang K, Yao X, Liu B, Ren B (2021) Metallic Plasmonic Array Structures: Principles, Fabrications, Properties, and Applications. Adv Mater 33:2007988. https://doi.org/10.1002/adma.202007988

2. Amendola V, Pilot R, Frasconi M, Maragò OM, Iatì MA (2017) Surface plasmon resonance in gold nanoparticles: a review. J Phys: Condens Matter 29:203002. https://doi.org/10.1088/1361-648X/aa60f3

3. Jang YH, Jang YJ, Kim S, Quan LN, Chung K, Kim DH (2016) Plasmonic Solar Cells: From Rational Design to Mechanism Overview. Chem Rev 116:14982–15034. https://doi.org/10.1021/acs.chemrev.6b00302

4. Anthony SP, Porel S, Rao DN, Radhakrishnan TP (2005) Thin films of metal-organic compounds and metal nanoparticle-embedded polymers for nonlinear optical applications. Pramana - J Phys 65:871–879. https://doi.org/10.1007/BF02704087

5. Omar R, En Naciri A, Jradi S, Battie Y, Toufaily J, Mortada H, Akil S (2017) One-step synthesis of a monolayer of monodisperse gold nanocubes for SERS substrates. J Mater Chem C 5:10813–10821. https://doi.org/10.1039/C7TC03069J

6. Zhang Y, Liu Q, Mundoor H, Yuan Y, Smalyukh II (2015) Metal Nanoparticle Dispersion, Alignment, and Assembly in Nematic Liquid Crystals for Applications in Switchable Plasmonic Color Filters and E-Polarizers. ACS Nano 9:3097–3108. https://doi.org/10.1021/nn5074644

7. Saito R, Okamura S, Ishizu K (1992) Introduction of colloidal silver into a poly(2-vinyl pyridine) microdomain of microphase separated poly(styrene-b-2-vinyl pyridine) film. Polymer 33:1099–1101. https://doi.org/10.1016/0032-3861(92)90029-V

8. Besson S, Gacoin T, Ricolleau C, Boilot J-P (2003) Silver nanoparticle growth in 3D-hexagonal mesoporous silica films. Chem Commun 360–361. https://doi.org/10.1039/b208357d

9. Miyama T, Yonezawa Y (2004) Photoinduced formation and aggregation of silver nanoparticles at the surface of carboxymethylcellulose films. J Nanopart Res 6:457–465. https://doi.org/10.1007/s11051-004-1716-1

10. Porel S, Singh S, Harsha SS, Rao DN, Radhakrishnan TP (2005) Nanoparticle-Embedded Polymer: In Situ Synthesis, Free-Standing Films with Highly Monodisperse Silver Nanoparticles and Optical Limiting. Chem Mater 17:9–12. https://doi.org/10.1021/cm0485963

11. Mohan YM, Premkumar T, Lee K, Geckeler KE (2006) Fabrication of Silver Nanoparticles in Hydrogel Networks. Macromol Rapid Commun 27:1346–1354. https://doi.org/10.1002/marc.200600297

12. Zhu J-F, Zhu Y-J (2006) Microwave-Assisted One-Step Synthesis of Polyacrylamide−Metal (M = Ag, Pt, Cu) Nanocomposites in Ethylene Glycol. J Phys Chem B 110:8593–8597. https://doi.org/10.1021/jp060488b

13. Zhang J, Dong W, Sheng J, Zheng J, Li J, Qiao L, Jiang L (2008) Silver nanoclusters formation in ion-exchanged glasses by thermal annealing, UV-laser and X-ray irradiation. Journal of Crystal Growth 310:234–239. https://doi.org/10.1016/j.jcrysgro.2007.10.007

14. Battie Y, Destouches N, Bois L, Chassagneux F, Tishchenko A, Parola S, Boukenter A (2010) Growth Mechanisms and Kinetics of Photoinduced Silver Nanoparticles in Mesostructured Hybrid Silica Films under UV and Visible Illumination. J Phys Chem C 114:8679–8687. https://doi.org/10.1021/jp9046903

15. Battie Y, Destouches N, Bois L, Chassagneux F, Moncoffre N, Toulhoat N, Jamon D, Ouerdane Y, Parola S, Boukenter A (2010) Generation of an ordered layer of silver nanoparticles in mesostructured dielectric films. J Nanopart Res 12:1073–1082. https://doi.org/10.1007/s11051-009-9794-8

16. Battie Y, Destouches N, Chassagneux F, Jamon D, Bois L, Moncoffre N, Toulhoat N (2011) Optical properties of silver nanoparticles thermally grown in a mesostructured hybrid silica film. Opt Mater Express 1:1019. https://doi.org/10.1364/OME.1.001019

17. Li S-M, Jia N, Ma M-G, Zhang Z, Liu Q-H, Sun R-C (2011) Cellulose–silver nanocomposites: Microwave-assisted synthesis, characterization, their thermal stability, and antimicrobial property. Carbohydrate Polymers 86:441–447. https://doi.org/10.1016/j.carbpol.2011.04.060

18. Destouches N, Battie Y, Crespo-Monteiro N, Chassagneux F, Bois L, Bakhti S, Vocanson F, Toulhoat N, Moncoffre N, Epicier T (2013) Photo-directed organization of silver nanoparticles in mesostructured silica and titania films. J Nanopart Res 15:1422. https://doi.org/10.1007/s11051-013-1422-y

19. López-Miranda A, Viramontes-Gamboa G, López-Valdivieso A (2014) Silver nanostructures from Ag(CN) 2 − reduction by citrate ions in the presence of dodecyl sulfate and Cu2+ ions. Synthesis and characterization. J Nanopart Res 16:2244. https://doi.org/10.1007/s11051-014-2244-2

20. Oates TWH (2006) Real time spectroscopic ellipsometry of nanoparticle growth. Appl Phys Lett 88:213115. https://doi.org/10.1063/1.2206870

21. Oates TWH, Christalle E (2007) Real-Time Spectroscopic Ellipsometry of Silver Nanoparticle Formation in Poly(Vinyl Alcohol) Thin Films. J Phys Chem C 111:182–187. https://doi.org/10.1021/jp065081l

22. Oates TWH, Wormeester H, Arwin H (2011) Characterization of plasmonic effects in thin films and metamaterials using spectroscopic ellipsometry. Progress in Surface Science 86:328–376. https://doi.org/10.1016/j.progsurf.2011.08.004

23. Voué M, Dahmouchène N, De Coninck J (2011) Annealing of polymer films with embedded silver nanoparticles: Effect on optical properties. Thin Solid Films 519:2963–2967. https://doi.org/10.1016/j.tsf.2010.12.109

24. Resano-Garcia A, Battie Y, En Naciri A, Akil S, Chaoui N (2015) Experimental and theoretical determination of the plasmonic responses and shape distribution of colloidal metallic nanoparticles. The Journal of Chemical Physics 142:134108. https://doi.org/10.1063/1.4916917

25. Battie Y, Izquierdo-Lorenzo I, Resano-Garcia A, Naciri AE, Akil S, Adam PM, Jradi S (2016) How to determine the morphology of plasmonic nanocrystals without transmission electron microscopy? J Nanopart Res 18:217. https://doi.org/10.1007/s11051-016-3533-8

26. Battie Y, En Naciri A, Vergnat M (2017) Plasmonic and metallic optical properties of Au/SiO_2 metal-insulator films. Journal of Applied Physics 122:213101. https://doi.org/10.1063/1.5003302

27. Battie Y, En Naciri A, Chaoui N, Le Gall Y, Muller D, Carrada M, Mathiot D (2017) Plasmonic properties of implanted Ag nanoparticles in SiO_2 thin layer by spectroscopic ellipsometry. Journal of Applied Physics 122:085308. https://doi.org/10.1063/1.4989793

28. Resano-Garcia A, Battie Y, Naciri AE, Chaoui N (2016) Interaction of a converging laser beam with a Ag colloidal solution during the ablation of a Ag target in water. Nanotechnology 27:215705. https://doi.org/10.1088/0957-4484/27/21/215705

29. Broch L, Johann L, Stein N, Zimmer A, Beck R (2007) Real time *in situ* ellipsometric and gravimetric monitoring for electrochemistry experiments. Review of Scientific Instruments 78:064101. https://doi.org/10.1063/1.2743273

30. Broch L, Stein N, Zimmer A, Battie Y, Naciri AE (2014) Design of a real-time spectroscopic rotating compensator ellipsometer without systematic errors. Thin Solid Films 571:509–512. https://doi.org/10.1016/j.tsf.2013.11.138

31. Abelès F (1950) La théorie générale des couches minces. J Phys Radium 11:307–309. https://doi.org/10.1051/jphysrad:01950001107030700

32. Palik ED (1985) Handbook of Optical Constants of Solids. Elsevier, Burlington

33. Schnepf MJ, Mayer M, Kuttner C, Tebbe M, Wolf D, Dulle M, Altantzis T, Formanek P, Förster S, Bals S, König TAF, Fery A (2017) Nanorattles with tailored electric field enhancement. Nanoscale 9:9376–9385. https://doi.org/10.1039/C7NR02952G

34. Guyot C, Leclère P, Voué M (2020) Gold nanoparticles growing in a polymer matrix: What can we learn from spectroscopic imaging ellipsometry? Journal of Vacuum Science & Technology B 38:013602. https://doi.org/10.1116/1.5129578

35. Liz-Marzán LM (2006) Tailoring Surface Plasmons through the Morphology and Assembly of Metal Nanoparticles. Langmuir 22:32–41. https://doi.org/10.1021/la0513353

36. Kelly KL, Coronado E, Zhao LL, Schatz GC (2003) The Optical Properties of Metal Nanoparticles: The Influence of Size, Shape, and Dielectric Environment. J Phys Chem B 107:668–677. https://doi.org/10.1021/jp026731y

37. Lu X, Rycenga M, Skrabalak SE, Wiley B, Xia Y (2009) Chemical Synthesis of Novel Plasmonic Nanoparticles. Annu Rev Phys Chem 60:167–192. https://doi.org/10.1146/annurev.physchem.040808.090434

38. Blackman GN, Genov DA (2018) Bounds on quantum confinement effects in metal nanoparticles. Phys Rev B 97:115440. https://doi.org/10.1103/PhysRevB.97.115440

39. Azzam RM, Bashara NM (2003) Ellipsometry and polarized light, paperback ed., 5. impr. North-Holland, Amsterdam

40. Guyot C, Vandestrick P, Marenne I, Deparis O, Voué M (2019) Growth dynamics and light scattering of gold nanoparticles in situ synthesized at high concentration in thin polymer films. Beilstein J Nanotechnol 10:1768–1777. https://doi.org/10.3762/bjnano.10.172

41. Lawrence CJ (1988) The mechanics of spin coating of polymer films. Phys Fluids 31:2786. https://doi.org/10.1063/1.866986

42. LaMer VK, Dinegar RH (1950) Theory, Production and Mechanism of Formation of Monodispersed Hydrosols. J Am Chem Soc 72:4847–4854. https://doi.org/10.1021/ja01167a001

43. Kramers H (1926) Some remarks on the theory of absorption and refraction of x-rays. Nature 117:774--775

44. Kronig R de L (1926) On the theory of dispersion of x-rays. Josa 12:547--557

45. Grundmann M (2010) Kramers–Kronig Relations. In: The Physics of Semiconductors. Springer Berlin Heidelberg, Berlin, Heidelberg, pp 775–776

46. Fan X, Zheng W, Singh DJ (2014) Light scattering and surface plasmons on small spherical particles. Light Sci Appl 3:e179–e179. https://doi.org/10.1038/lsa.2014.60

47. Theiß W (1993) The use of effective medium theories in optical spectroscopy. In: Helbig R (ed) Advances in Solid State Physics 33. Springer Berlin Heidelberg, Berlin, Heidelberg, pp 149–176

48. Liu Z, Wang H, Li H, Wang X (1998) Red shift of plasmon resonance frequency due to the interacting Ag nanoparticles embedded in single crystal SiO2 by implantation. Applied Physics Letters 72:1823–1825. https://doi.org/10.1063/1.121196

49. Bernabò M, Pucci A, Galembeck F, Leite CA de P, Ruggeri G (2009) Thermal- and Sun-Promoted Generation of Silver Nanoparticles Embedded into Poly(vinyl alcohol) Films. Macromol Mater Eng 294:256–264. https://doi.org/10.1002/mame.200800330

50. Nicolais L, Carotenuto G (2014) Nanocomposites: in situ synthesis of polymer-embedded nanostructures, First edition. Wiley, Hoboken, New Jersey

51. Wilkes CE, Summers JW, Daniels CA, Berard MT (2005) PVC handbook. Hanser, Munich ; Cincinnati

52. Jain PK, Huang W, El-Sayed MA (2007) On the Universal Scaling Behavior of the Distance Decay of Plasmon Coupling in Metal Nanoparticle Pairs: A Plasmon Ruler Equation. Nano Lett 7:2080–2088. https://doi.org/10.1021/nl071008a

53. Tabor C, Murali R, Mahmoud M, El-Sayed MA (2009) On the Use of Plasmonic Nanoparticle Pairs As a Plasmon Ruler: The Dependence of the Near-Field Dipole Plasmon Coupling on Nanoparticle Size and Shape. J Phys Chem A 113:1946–1953. https://doi.org/10.1021/jp807904s

54. Encina ER, Coronado EA (2010) Plasmon Coupling in Silver Nanosphere Pairs. J Phys Chem C 114:3918–3923. https://doi.org/10.1021/jp912096v